SPECIAL ISSUE ARTICLE



Check for updates

Experimental and numerical determination of the fatigue notch factor in as-built wire arc additive manufacturing steel components

Davide Leonetti¹ | Elena Zancato¹ | Giovanni Meneghetti² | Johan Maljaars^{1,3}

Correspondence

Davide Leonetti, Department of The Built Environment, Eindhoven University of Technology, Eindhoven, The Netherlands. Email: d.leonetti@tue.nl

Funding information

None reported.

Abstract

Parts manufactured by wire arc additive manufacturing (WAAM) are characterized by a peculiar surface morphology, namely, surface waviness, that negatively affects the fatigue performance. To exploit the full potential of WAAM and minimize the need for postproduction work, it is crucial to utilize the components in the as-built state. This is because conventional machining techniques, typically employed for postprocessing operations, severely curtail the freedom of geometry of the components. This study focuses on an experimental and numerical characterization of the notch effect of the surface waviness for an AISI 308 LSi stainless steel. This is done by quantifying the fatigue notch factor in a probabilistic fashion, considering the results of ad-hoc designed fatigue tests. A finite element model is developed by considering a 3D scan of the geometry of WAAMed plates, allowing to determine the theoretical stress concentration factor. The fatigue notch factor is also estimated from the numerical model by making use of the gradient correction according to the FKM guidelines. To validate the numerical approach, test data produced for different testing conditions are correlated by using the local stress approach, showing that classical methods are also applicable to additive manufactured parts.

KEYWORDS

fatigue, notch effect, stainless steel, surface waviness, WAAM

1 | INTRODUCTION

Additive manufacturing (AM) is an increasingly utilized production technology in many industrial sectors. Wire arc additive manufacturing (WAAM) is a direct energy deposition technique that uses arc welding to manufacture components of various shapes. WAAM is currently

applied in several industrial sectors, for example, aerospace, automotive, construction, and marine.^{2–5} It combines great design freedom with high production rates, thanks to higher deposition rates as compared to other metal AM processes. WAAM is based on the successive deposition of weld beads onto each other resulting in a layered structure.⁶ Generally, AM is considered

This is an open access article under the terms of the Creative Commons Attribution-NonCommercial License, which permits use, distribution and reproduction in any medium, provided the original work is properly cited and is not used for commercial purposes.

© 2024 The Author(s). Fatigue & Fracture of Engineering Materials & Structures published by John Wiley & Sons Ltd.

¹Department of The Built Environment, Eindhoven University of Technology, Eindhoven, The Netherlands

²Department of Industrial Engineering, University of Padova, Padova, Italy ³TNO Delft, Delft, The Netherlands

advantageous in terms of material usage since it can effectively reduce waste for complex geometries. However, for structural applications, it is relevant to understand the effect of the as-built surface on fatigue failure. This is because the quality of the surface plays a relevant role in crack initiation. Due to the layer-by-layer deposition of weld beads, the surface irregularities of WAAMed structural elements, hereafter referred to as surface waviness, are affected by the process parameters.⁸ Several studies are devoted to the improvement of the surface of WAAMed components by different methods, 8 including machining⁹ and rolling.¹⁰

To utilize WAAMed components in the as-built condition as much as possible, the effect of the as-built surface on the structural integrity of WAAMed components is of relevance. Hence, there is a need for minimizing additional, expensive, and time-consuming manufacturing steps, such as surface treatments or material removal processes, leading to several studies focusing on the structural integrity of WAAMed components. In some studies, this has been approached considering that the material has internal defects due to manufacturing. For example, in Biswal et al, 11 the effect of pores on the fatigue strength of a WAAMed Ti-alloy has been studied and explained in terms of fracture mechanics. These studies extend beyond WAAMed components and are generally applicable to other AM processes, such as powder bed fusion, 12 and selective laser melting. 13

Considering the high-cycle fatigue regime, in the absence of superficial defects, such as lack of fusion and cold cracks, crack initiation at the surface is potentially a dominant failure mechanism as compared to crack initiation at a sub-superficial defect, as in the case of welded joints. 14 Therefore, when superficial crack-like defects are not present, the notch effect induced by the as-built surface is dominating, and it is a limiting factor for the widespread applicability of WAAM.

With regards to fatigue characterization of WAAMed components, only a limited number of studies are available, 15-21 and this number is further reduced when considering the effect of as-built surface notches on the fatigue strength of WAAMed components. Bartsch et al²² conducted an experimental and numerical investigation for the determination of the strength of WAAMed components characterized by an as-built surface. They proposed to use the effective notch stress concept for numerically estimating the notch effect for flat specimens under axial loading. The effective notch stress concept, as employed in Bartsch et al,²² is based on an effective radius equal to 0.05 mm considering an S-N curve identified by FAT630, which is used for plate thickness less than 5 mm. 23,24 In Shamir et al, 25 an experimental comparison between WAAMed components with and

without the surface in the as-built condition is conducted by testing the specimens in a three-point bending setup. The authors estimated the effect of the surface waviness by considering a single wave. They used the resulting theoretical stress concentration factor, K_t , to estimate the notch effect due to the as-built surface, hence without considering the microstructural support and stress gradient effects. Alternatively, it was shown that a fracture mechanics approach gives acceptable predictions when the surface is as-built. This has been addressed to the predominance of the crack growth phase over the crack nucleation phase.

Other studies focusing on the effect of the as-built surface on the fatigue strength of AM components make use of more advanced local stress approaches, like in Huang et al.¹⁹ These methods have been referred to as local approaches and have been developed for assessing welded joints²⁶ and structural components.²⁷

Using continuum mechanics, the quantification of the notch effect involves the empirical determination of the fatigue notch factor, K_f , which is experimentally determined as the ratio between the endurance limit of smooth components and notched components. This is different than done in the literature, 11,13 where notch factors are based on fracture mechanics. The notch factor should be smaller than the (linear elastic) stress concentration factor, 26 $K_f < K_t$, which implies that the stress amplitude to be used for fatigue calculation is smaller than the theoretical stress amplitude at a given stress ratio, $\sigma_{a,f,R} < \sigma_{a,t,R}$. In Hensel et al, ¹⁸ the fatigue notch factor, K_f , is estimated between 1.34 and 2.00, for specimens extracted in the direction perpendicular to the deposition plane and made of AM80 produced by direct energy deposition. Values in a similar range, that is between 1.55 and 2.16, have been analytically evaluated by Huang et al, 19 for a WAAMed thin-wall component made of ER70S-6. However, in all the above-mentioned cases, the specimens are produced by using a linear printing pattern, which results in a different surface morphology as compared to a zig-zag printing pattern that is used for manufacture relatively thick components.

In this paper, the fatigue notch factor due to the asbuilt surface is evaluated through an experimental campaign consisting of fatigue tests conducted on specimens extracted from WAAMed plates made of AISI 308 LSi stainless steel grade, by considering a load ratio R = 0.1. The uniaxial cyclic load has been applied normally to the deposition plane, since this direction is the one resulting in the highest stress concentration. As compared to other experimental studies available in the scientific literature, in this paper (a) a novel design of the specimens is presented, aiming to preserve the notch effect in as-built WAAM components, (b) the fatigue notch factor is estimated for specimens extracted from relatively thick plates for which a zig-zag printing pattern has been used, and (c) a statistical description of the fatigue notch factor is provided. Furthermore, the research presents an analysis of the fracture surfaces of the broken specimens through a scanning electron microscope (SEM). Subsequently, a numerical evaluation of the fatigue notch factor is conducted by using a finite element model. The method proposed in the FKM guideline²⁷ is used to take into account the effect of the stress gradient and the microstructural support, thus enabling applicability to other materials. The proposed framework is applied to three sets of tests conducted at different load ratios, that is R = 0.1, 0.5, and with smooth and as-built surface.

2 | MATERIALS AND EXPERIMENTS

This section describes the experiments conducted on the AISI 308 LSi stainless steel grade produced by WAAM. First, the specimen geometry and the experimental setup used to characterize the static tensile properties of the material are presented. Then, the staircase tests conducted to estimate the endurance limit of the material obtained in rotating bending fatigue tests are described. Finally, the fatigue tests performed to evaluate the notch effect are presented.

The plates from which the specimens are extracted are provided by the company MX3D²⁸ and are produced by using an AISI 308 LSi stainless steel grade drawn wire with a diameter of 1.2 mm and the settings reported in Table 1, where the maximum dimensions of the plates are also reported. The geometry of the plates used for the

TABLE 1 Printing settings used for the production of the plates.

Setting	Value	Unit
Current	109	A
Wire feeding speed	3.7	m/min
Shielding gas	98% Ar + 2% CO	O_2
Layer height	2.3	mm
Arc length	2.0	mm
Welding mode	Pulsed	
Strategy	zig-zag+edge su	pport
Interpass temperature	200	Celsius
Plate	Dimension (B × H	× T) Unit
Tensile specimens	$200\times200\times20$	mm
Axial fatigue specimens	$470 \times 200 \times 16$	mm
Rotating bending	$400 \times 160 \times 17$	mm

production of the axial fatigue specimens is shown in Figure 1, in which the plane identified by the X and Z axes is the deposition plane, and the Y axis identifies the building direction. A total of 52 layers are deposited to manufacture each plate. As indicated in Table 1, the plates are fabricated by using a zig-zag printing pattern within the deposition plane, see Figure 1, which is commonly used for the production of components larger than a single layer.²⁹

The specimens are extracted from the plates first by waterjet cutting and successively machined to the final dimension and shape. This is a typical procedure employed for characterizing the material properties of WAAM parts.³⁰ This is different than for other AM techniques, for example, laser powder bed fusion, in which specimens are directly manufactured. For WAAM, this step is necessary for several reasons: (a) to limit distortion of relatively small parts, and (b) to study the effect of different printing patterns typical of larger components, which cannot be reproduced on small-scale specimens. By using waterjet cutting, the heat input induced by the extraction procedure is minimized as compared to laser or saw cutting. The specimens used to characterize monotonic properties and fatigue strength are extracted

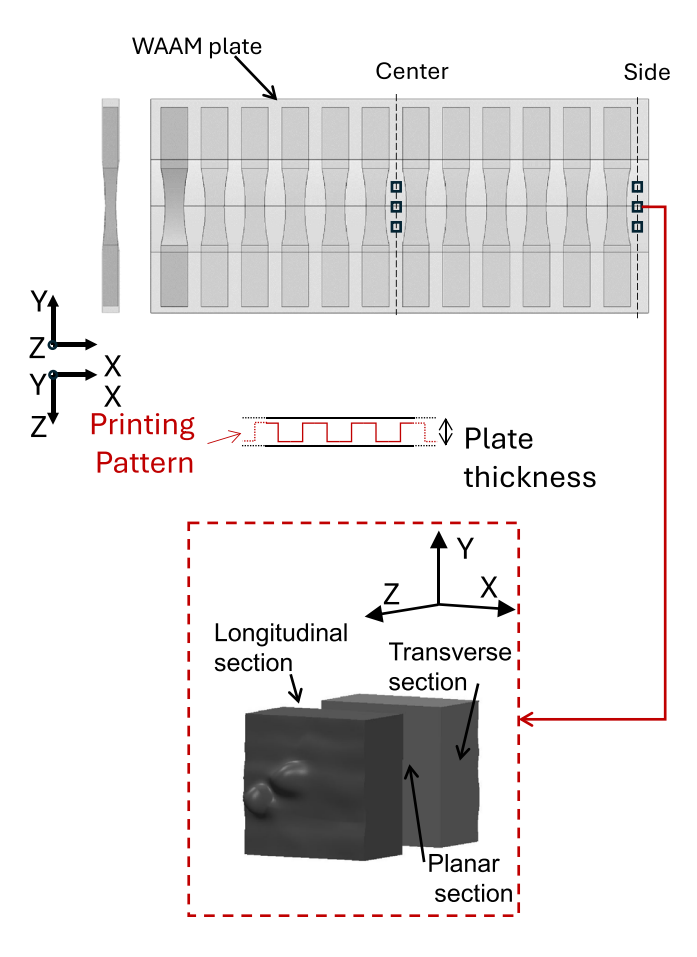


FIGURE 1 Specimen orientation within a plate and printing pattern. [Colour figure can be viewed at wileyonlinelibrary.com]

so that the deposition plane is perpendicular to the longitudinal axis of the specimen, the latter being coincident with the loading direction. This is shown for the fatigue specimens in Figure 1. On the basis of previous observations, 22,25 this configuration is the weakest for two reasons: (1) the highest stress concentration resulting from the surface waviness, due to its geometrical configuration, and (2) the material behavior observed from smooth specimens results in lower static and fatigue strength. 20,30

Monotonic tensile tests and 2.1 hardness

The static tensile tests are executed on cylindrical specimens designed in accordance with the specifications given in ASTM-E8M.³¹ The specimens are taken from the middle section of the plate, first extracted by waterjet cutting, and then entirely machined at the lathe. Therefore, they are employed to characterize the material, and not the effect of the as-built surface. The specimens have a circular cross-section with a diameter of 9.0 mm and a parallel length of 45.0 mm, and it is shown in Figure 2. The nominal gage length used to measure the axial strain is 40 mm. The tests are conducted by using an Instron 5985 universal testing machine having a capacity of 250 kN. The testing machine is equipped with a 250 kN

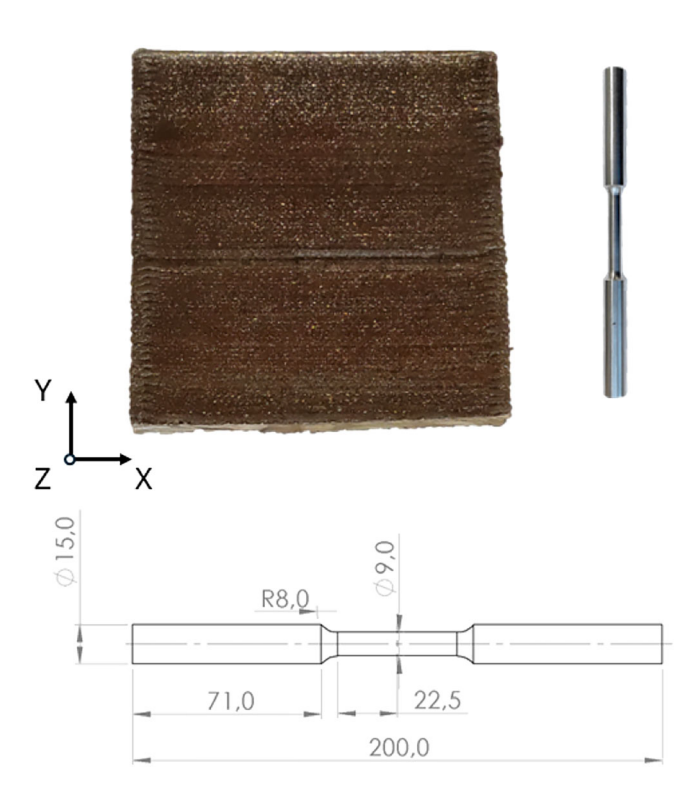


FIGURE 2 Plate used to extract specimens for tensile tests. [Colour figure can be viewed at wileyonlinelibrary.com]

force transducer and the AVE2 contactless extensometer. A total of eight tests are conducted at a displacement rate of 0.6 mm/min.

From the same plates, metallographic samples are extracted to observe potential differences in the microstructure on the planar, longitudinal, and transverse sections at the center and the end of the plates, see Figure 1. The same specimens are used for the measurement of Vickers hardness. This allows for the identification of different microstructures resulting from different thermal cycles during the printing process, due to different cooling rates of the edges and the central part of the plate and between layers. For each section, the surfaces are examined under an optical Leica DMRE microscope, according to the ASTM-E3 standard. 32 The rolling direction indicated in the ASTM-E3 standard is replaced with the direction identified by the intersection of the deposition plane and the front plane of each plate. The samples are ground and polished, and subsequently subjected to electrolytic etching by using a compound consisting of 10% aqueous oxalic acid $(HO_2C - CO_2H)$ and a voltage of 6V. An immersion time of 30 s is applied.

2.2 Staircase tests

The staircase method is used to determine the fatigue strength at 10⁷ cycles. The specimens are sequentially tested under increasing stresses until failure occurs, otherwise the stress level is decreased. In these tests, the initial stress level is the expected stress amplitude at the endurance limit, that is, 260 MPa, and the considered step range is 10 MPa, that is, 3.8% of the expected value at the endurance limit. The expected stress amplitude at the endurance limit is based on the results of rotating bending tests conducted on the same material.²⁰ The tests are conducted by using a rotating bending testing machine model RB35 from Italsigma capable of applying between 8 and 35 Nm. As for the specimens used in the static tensile tests, they are taken from the middle section of the plate, first extracted by waterjet cutting, and then entirely machined at the lathe. An hourglass shape has been selected to manufacture the cylindrical specimens. The critical cross section is characterized by a diameter of 7.5 mm, and it is machined at the lathe reaching a surface quality Ra = 1.6 and successively finegrounded. The choice of an hourglass shape is driven by the observation that this material is prone to self-heating.²⁰ In fact, as compared to specimens with uniform cross-sections, in hourglass specimens the cross-sections adjacent to the critical cross-section are characterized by lower stress amplitudes and stress rates, hence reducing the effects of self-heating due to the limited volume of material subjected to the highest stress amplitude, and stress rate. This phenomenon is emphasized by the lower thermal conductivity of AISI 308 LSi steel grade compared to carbon steel. Moreover, the rotational speed adopted in the present investigation has been limited to 5000 rpm, which proved to effectively avoid overheating according to surface temperature measurements performed with a pyrometer, and at the same time led to reasonable testing time. This way, the heat generated during the test is minimized.

2.3 | Fatigue tests

The tests are conducted in a hydraulic testing bench from Schenck with a capacity of 400 kN and equipped with self-centering wedge grips. Two load ratios are considered for the experiments, that is R = 0.1 and 0.5.

High-cycle fatigue tests are conducted on two series of specimens and the number of cycles to failure is reported at complete specimen separation. More precisely, in one series, the as-built surface has been preserved, whereas in the second series, the as-built surface has been machined of comparable quality as for the staircase tests, that is, Ra = 1.6.

Different from other investigations available in the literature, for example, Bartsch et al,²² which make use of flat specimens with dog-bone shape, the specimens used in this work are characterized by an hourglass shape both in the frontal and the side plane. Therefore, the design of the specimen is such that failure occurs in the

mid-section of the specimen. The choice of an hourglass shape in both planes is motivated by the observation that the surface waviness, on which this study is focused, can be modeled as a series of periodic notches. This way, fatigue failure is avoided at the first notch, which is the first wave adjacent to the grip area. For periodic notches in uniform plates, the first notch is characterized by a higher theoretical stress concentration factor K_t than the other notches.³³ Failure at the first notch resulting from surface waviness is likely to be not relevant for real structures for two reasons: (a) the geometry is generally more complex than that of a uniaxial specimen and abrupt geometric discontinuities are usually avoided so that a first notch does not exist, (b) even if a first notch exists, the internal force and the associated stress distribution in a real structure are usually nonuniform such, that the first notch is not critical. Hence, the hourglass shape ensures that the ratio between the nominal stress at the grip area and the nominal stress at the center of the specimen is larger than the ratio between the theoretical stress concentration factor for the first notch and the theoretical stress concentration factor for the other notches. By taking advantage of the freedom of virtually manufacturing any shape, the plates used for the extraction of the fatigue specimens are produced in an hourglass shape in the YZ plane, as depicted in Figures 1 and 3A. While extracting the specimens, an hourglass shape is also made for the XY plane, as shown in Figure 3B,C. Thus, the specimens are thicker and wider in correspondence to grip sections, and thinner and narrower in correspondence with the test section, allowing the preservation of the as-built

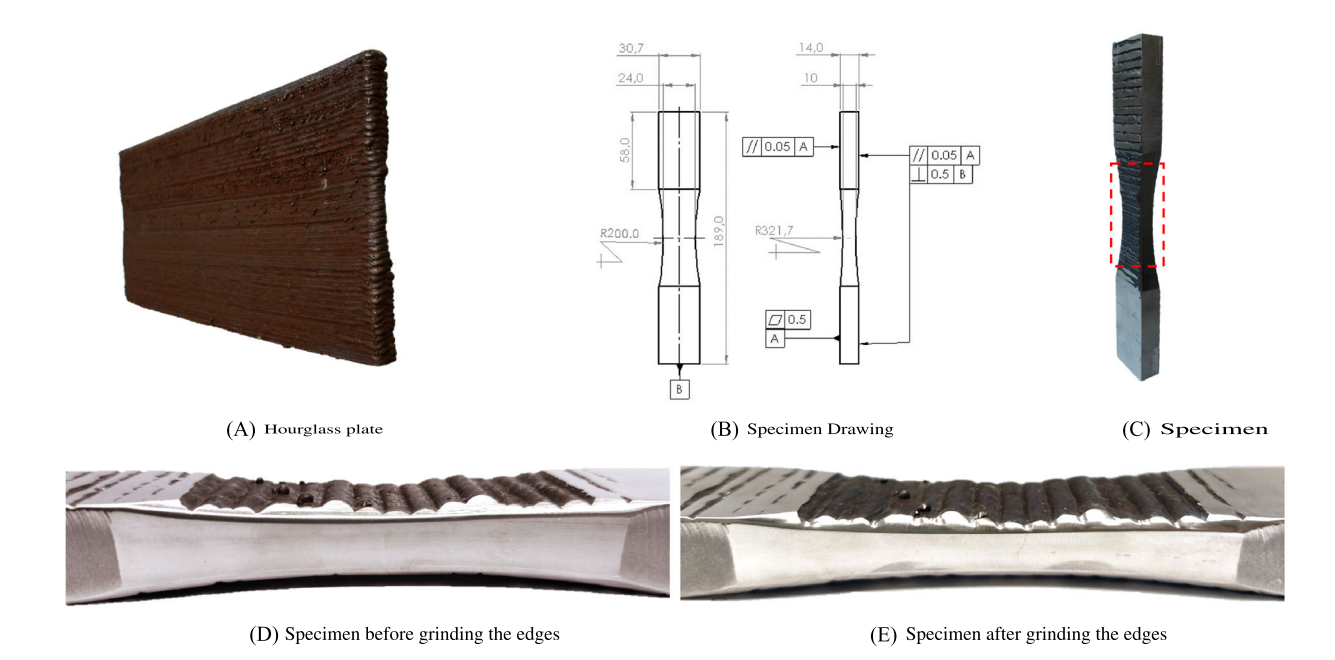


FIGURE 3 Extraction and shape of the as-built specimen used for the fatigue tests. [Colour figure can be viewed at wileyonlinelibrary.com]

surface condition in the mid-section. In addition, to avoid the risk of failure at the end of each of the grip sections, the hourglass shape also enables the possibility of milling the clamped ends of the specimen to enhance grip.

The sides of the specimens are also machined and characterized by a surface roughness Ra = 1.6. Once the specimens are extracted, the cuspids formed by the intersection of the as-built surface with the sides of the specimens are ground with a grinding stone having 800 grit and a conical shape. The result of this procedure is shown in Figure 3, where the as-built surface is depicted in Figure 3C, and the side of the specimen is shown in Figures 3D,E before and after grinding, respectively. This has several beneficial effects against the occurrence of crack initiation at the cuspids formed by the intersection of the as-built surface with the sides of the specimen. In particular: (1) by rounding the deepest point of the notches with the tip of the conical grinding stone, the stress concentration in correspondence with the edges of the specimens is reduced, (2) the grinding wheel ensures that the grinding direction is parallel with the loading direction, thus grinding marks are parallel to the loading direction and do not significantly induce stress concentration as compared to transverse marks, (3) the sharpness of the edge is reduced to a curvature, increasing the confinement of the slip of the grains at this location, as suggested in the ASTM E466 standard.³⁴ The notch effect is obtained by comparing the S-N curves of smooth and as-built specimens for R = 0.1. The S-N curve obtained for as-built specimens at R = 0.5 provides a reference curve for the design of WAAMed components in the presence of tensile residual stresses. Moreover, analyzing the test results obtained at R = 0.1 and R = 0.5allows to explore the applicability of commonly used mean stress correction rules.

3 **MODELS**

This section presents the formulation of a FE model aiming at a numerical determination of the notch effect resulting from the as-built surface. Therefore, the first section presents the finite element model developed in the ANSYS Workbench³⁵ environment, whereas the second section presents the framework used for fatigue life estimation.

3.1 FE model

The FE model presented in this section is used for the determination of the stress concentration factor and stress gradient at the most stressed location due to the

waviness of the as-built surface. The FE model is formulated based on the geometry of the plates used to conduct the fatigue tests. To do this, the surfaces of the plates are scanned and used to build the model geometry. The scans are made with a Wenzel LH65 coordinate measuring machine equipped with a Nikon L100 3D scanner. The setup allows reaching measurement error below 50 μm, and a probing error below 6.5 µm. The scans are conducted in a room at a controlled temperature, where the temperature of the plates is deemed to be uniform and constant. For each plate, multiple measurements are conducted by scanning in different directions, as compared to the weld beads, namely, 0°,90°,180°,270°, with the probe oriented with a 45° direction to the plate. This way, it is possible to correctly digitize the morphological features of the plates such as weld spatters or deeper grooves which, due to their geometry, are not possible to digitize with a single scan from only one direction. Following different scans, the point clouds are combined into a unique surface in a STL file.

Due to the large amount of points per plate, further processing of the acquired point cloud is done in Poliworks³⁶ software to reduce the number of points without losing the accuracy of the waviness and local features. The software uses an adaptive strategy in which, as a result, the points are omitted whenever their omission does not significantly alter the geometry. Therefore, more points are left when the curvature radius is smaller.

The scanned surface is imported into ANSYS Workbench³⁵ software and a solid geometric model is created in the CAD environment within ANSYS Workbench starting from the STL file. More precisely, a plane is identified by interpolating the points located on the grip areas of the plate. Then, the surface is extruded up to a plane located at 8 mm to the aforementioned reference plane, because the nominal thickness of the plates in correspondence with the grip area is 16 mm. This way, half of the plate is modeled considering the symmetry plane of the nominal geometry, which is oriented as a planar section as indicated in Figure 1. Modeling half plate and applying symmetry boundary conditions in the nominal symmetry plane of the FE model is based on the assumption that the uneven waviness of the as-built surfaces only affects local stress concentration and not the global stress distribution, that is, excluding notch effect. In other words, the effect of uneven waviness is assumed to cause only uneven local stress concentrations and a secondary bending moment. Finally, the grip sections have been not modeled, leaving only the hourglass portion of the plate, which is shown in Figure 4A.

The finite element solution to obtain the fatigue notch factor due to the as-built surface is obtained by the submodeling technique. It is used because of the

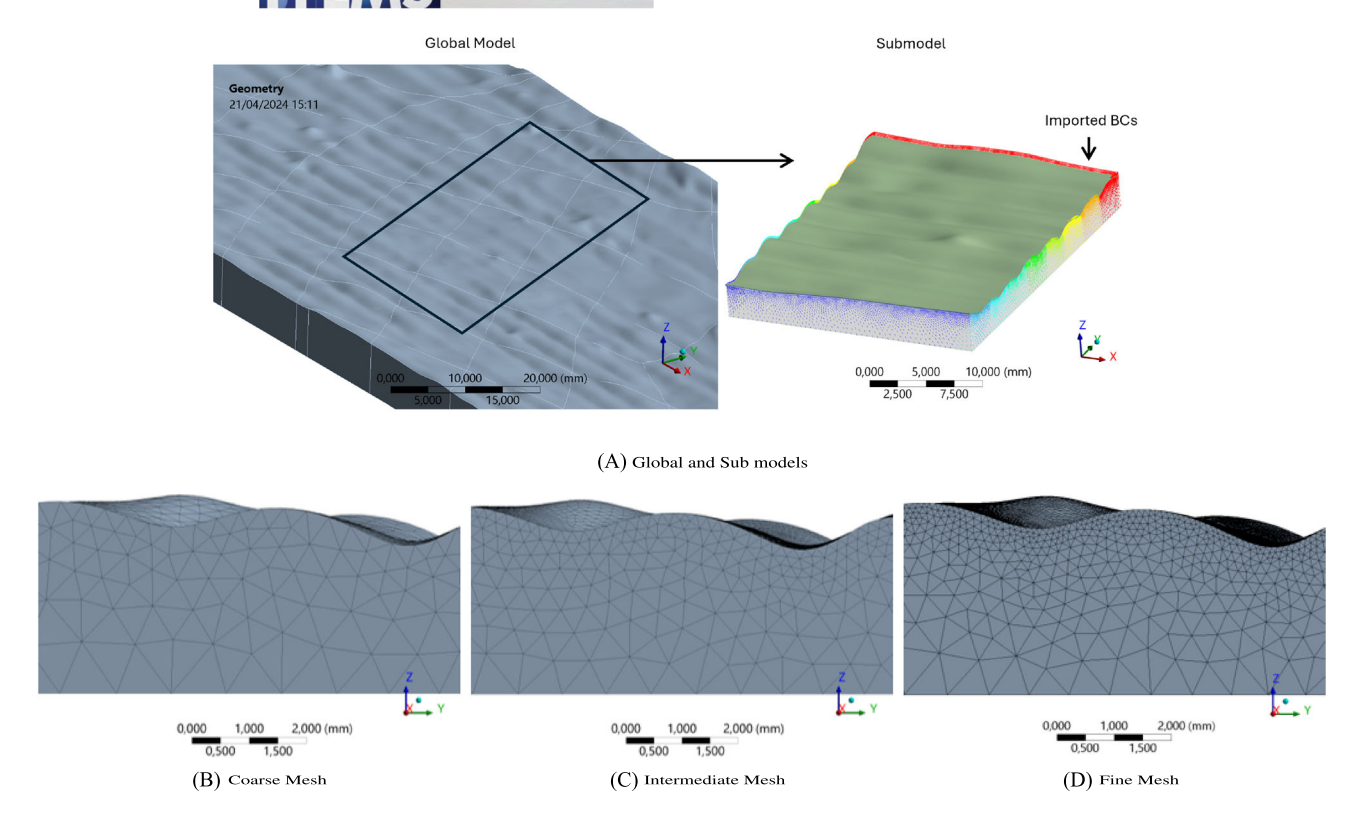


FIGURE 4 Geometry of the plate imported in Ansys and example of the submodel (A) and mesh discretization (B–D). [Colour figure can be viewed at wileyonlinelibrary.com]

large number of mesh nodes required to accurately model the stress concentration factor for a certain portion of the as-built surface through the whole plate. The procedure is presented in the next section. Within the submodeling technique, the nodal displacements resulting from the solution of a finite element model of the entire plate characterized by a relatively coarse mesh, that is, a global model, are mapped and applied to the boundaries of the submodel, as shown in Figure 4A. Since the submodel is characterized by a finer mesh discretization, this allows to reduce the computational effort of the analysis.

Both the global model and submodel have been discretized by using 10-node tetrahedral elements with quadratic displacement functions. The material used is a linear elastic material with Young's modulus equal to 200 GPa and a Poisson ratio equal to 0.3. The global model is constrained by using symmetry boundary conditions at the symmetry plane. The load is applied to the model through a uniform distribution of nodal forces. The magnitude of the resulting force is such that the average stress at the nominal net section is unitary. Hence, a uniform stress of 0.70 MPa is applied in the remote cross-section. In addition, the surface opposite to the one where the load is applied is constrained to suppress normal displacements.

For the submodel, the boundary conditions are imported from the global model for all the surfaces except for the as-built one. Three sizes are considered for the mesh convergence study, namely, a coarse, intermediate, and fine mesh, depicted in Figure 4B–D. The different mesh sizes are generated by assigning an element size to the as-built surface and selecting a mesh growth rate of 1.2 by using the MOPT command in ANSYS, meaning that the size of adjacent elements cannot differ for more than 20%. This provides a smooth transition of the mesh element size as a function of the distance from the as-built surface. The selected element sizes at the surface are 0.1, 0.2, and 0.4 for the fine, intermediate, and coarse mesh, respectively. The element size in the submodel is never larger than 2 mm.

The convergence study is conducted on the submodel located at the center of the plate by comparing the maximum principal stress and its gradient at the most stressed location identified by the model with the finest discretization. The study revealed that a difference smaller than 5% results when comparing the output of the intermediate and the fine mesh, which is considered acceptable. Due to the variability of the as-built surface, a more severe condition could exist in another location. To deal with this, the fine mesh is selected for carrying out the analysis. This way, the variability of the surface waviness is addressed while choosing the mesh size.

3.2 | Estimation of fatigue notch factor

The estimation of the fatigue notch factor is performed considering the results of the submodel. The analysis starts with the identification of the node on the as-built surface resulting in the highest stress concentration factor, considering the maximum principal stress and averaged nodal results. In particular, to avoid unwanted load introduction effects, the results of the first two rows of elements from the boundary, that is, any element with a node on the boundary and any adjacent one to these, are disregarded.

The fatigue notch factor is calculated considering the procedure recommended in the FKM guidelines.²⁷ This procedure involves the estimation of the maximum principal stress gradient, G_{σ} , at the most stressed location, along the direction perpendicular to that one of the maximum principal stress. The stress gradient is used to compute the ratio, n_{σ} , between the theoretical stress concentration factor, K_t , and the fatigue notch factor, K_f , considering material-dependent parameters. Therefore, since both K_t and the normalized stress gradient are an output of the FE model, the fatigue notch factor K_f can be determined. To accomplish the procedure just outlined, a script is developed in ANSYS MAPDL³⁵ environment, performing the following steps, which is also visualized in Figure 5, that is,

- 1. The most stressed location within the submodel is identified and the maximum principal stress $\sigma_{1,p}$ is evaluated at the as-built surface, corresponding to the node p. This corresponds to the root of the notch introduced by the surface waviness as shown in Figure 5.
- 2. Since $\sigma_{1,p}$ is tangent to the surface at the notch root, the stress gradient is evaluated normal to the surface. To identify this, the elements connected to node p are

considered. Through a search procedure, a triplet of nodes maximizing the perimeter of the triangle of which they are the vertices is found among the nodes of the aforementioned elements. This triplet, as shown in Figure 5, is used to identify the plane π of equation $a_{\pi} \cdot x + b_{\pi} \cdot y + c_{\pi} \cdot z + d_{\pi} = 0$ for which the normal direction can be calculated, considering the location of the node p, that is, (x_p, y_p, z_p) :

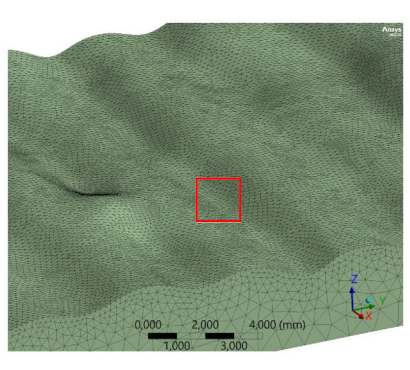
$$\begin{cases} x = x_p + a_{\pi} \cdot t \\ y = y_p + b_{\pi} \cdot t \\ z = z_p + c_{\pi} \cdot t \end{cases}$$
 (1)

The numerical approximation of the tangent plane π is dependent on the mesh size. However, as shown in Section 3.1, it is checked that the selected mesh size provides a convergent approximation of the tangent plane.

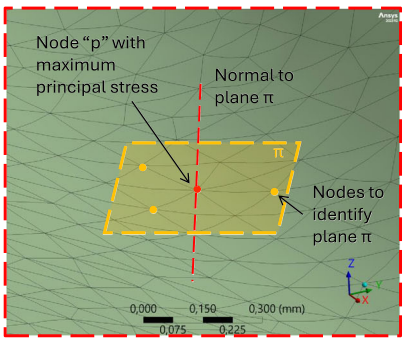
3. The determination of the stress gradient requires the maximum principal stress to be evaluated along the normal direction at a certain distance from node p and ensuring that the stress distribution can be locally approximated by a straight line. Once this point $k \equiv (x_k, y_k, z_k)$ is found, the distance is evaluated as

$$\Delta s = \sqrt{(x_p - x_k)^2 + (y_p - y_k)^2 + (z_p - z_k)^2}$$
 (2)

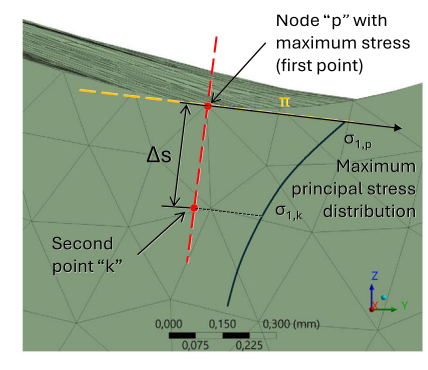
Starting from an arbitrarily large distance of 5 mm, the location at which $\sigma_{1,k}$ is evaluated is identified by the bisection method in such a way that the procedure stops when this location is within a linear region of the stress distribution. The maximum principal stress at each location is extracted by interpolating nodal results, thus determining $\sigma_{1,k}$.



(A) As-built surface in submodel



(B) Closer view



(C) Section view

FIGURE 5 Procedure used to determine the fatigue notch factor according to FKM. [Colour figure can be viewed at wileyonlinelibrary.com]

4. The normalized stress gradient of the maximum principal stress, G_{σ} , is calculated as

$$G_{\sigma} = \frac{1}{\Delta s} \left(1 - \frac{\sigma_{1,k}}{\sigma_{1,p}} \right) \tag{3}$$

5. Successively, the value of n_{σ} , that is, the ratio between K_t and K_f for normal stresses, is

$$n_{\sigma} = \begin{cases} n_{\sigma} = 1 + G_{\sigma} \cdot 10^{-\left(a_{G} - 0.5 + \frac{\sigma_{u}}{b_{G}}\right)} & \text{if } G_{\sigma} \leq 0.1^{-1} \\ n_{\sigma} = 1 + \sqrt{G_{\sigma}} \cdot 10^{-\left(a_{G} + \frac{\sigma_{u}}{b_{G}}\right)} & \text{if } 0.1^{-1} < G_{\sigma} \leq 1 \text{mm}^{-1} \\ n_{\sigma} = 1 + \sqrt[4]{G_{\sigma}} \cdot 10^{-\left(a_{G} + \frac{\sigma_{u}}{b_{G}}\right)} & \text{if } 1^{-1} < G_{\sigma} \leq 100 \text{mm}^{-1} \end{cases}$$

$$(44)$$

in which $a_G = 0.40$ and $b_G = 2400$ are material-dependent parameters provided in FKM guideline for stainless steel,²⁷ and σ_u is the ultimate tensile stress.

6. Calculate the value of K_f as

$$K_f = \frac{K_t}{n_\sigma} = \frac{\sigma_{1,k}}{\sigma_{nom} \cdot n_\sigma} \tag{5}$$

where σ_{nom} =1 MPa is the average stress in the nominal net cross-section.

Finally, the aforementioned procedure makes it possible to estimate the value of K_f and to perform fatigue life estimation considering the S-N curve for smooth specimens. Moreover, by considering different locations for the submodel along the plate, the variation of the fatigue notch factor can be evaluated. In particular, the submodel has the same width as the test specimen.

3.3 | Estimation of endurance limit

To evaluate the predictive capability of the numerically determined fatigue notch factor, this is also experimentally determined as the ratio between the fatigue resistance of the smooth specimens and the fatigue resistance of the as-built specimens. All the experimental data are corrected considering the fatigue notch factor obtained experimentally. Hence, by considering both the obtained value of K_f and a mean stress correction rule, the local fatigue stress can be calculated for all the test specimens for a unique stress ratio that for simplicity is set to R = -1.

The local fatigue stress amplitude and maximum values are calculated by

$$\sigma_{a,f,R} = K_f \cdot \frac{\Delta \sigma_{nom,R}}{2} \tag{6}$$

$$\sigma_{max,f,R} = K_f \cdot \frac{\Delta \sigma_{nom,R}}{1 - R} \tag{7}$$

Note that $K_f=1$ is for smooth specimens. Considering that locally elastic shakedown takes place and assuming an elastic perfectly plastic material, that is, when $\sigma_{max,f,R}>\sigma_{p,0.2}$ and $\sigma_{a,f,R}<\sigma_{p,0.2}$, where $\sigma_{p,0.2}$ is the 0.2% proof stress, the effective mean stress can be determined by assuming that the maximum stress does not exceed the yield stress:

$$R_{eff,sh} = \frac{\sigma_{p,0.2} - (K_f \cdot \Delta \sigma_{nom,R})}{\sigma_{p,0.2}} \tag{8}$$

meaning that locally, the effective stress ratio could differ from the stress ratio of the nominal stress. Based on the aforementioned assumption, the corrected mean stress is calculated as $\sigma_{mf,R}^* = \sigma_{p,0.2} - \sigma_{af,R}$. By using the Goodman mean stress correction, the equivalent stress amplitude for a load ratio R=-1 can be calculated as

$$\sigma_{a,f,R=-1} = \sigma_{a,f,R} \frac{\sigma_u}{\sigma_u - \sigma_{m,f,R}^*} \tag{9}$$

By calculating $\sigma_{a,f,R=-1}$ for all the experimental data points, the agreement of the experimental data is evaluated in terms of linear regression. This would validate the experimental fatigue notch factor and the use of the Goodman mean stress correction rule to correlate the considered loading conditions and the effect of the surface as reported in Section 2.3.

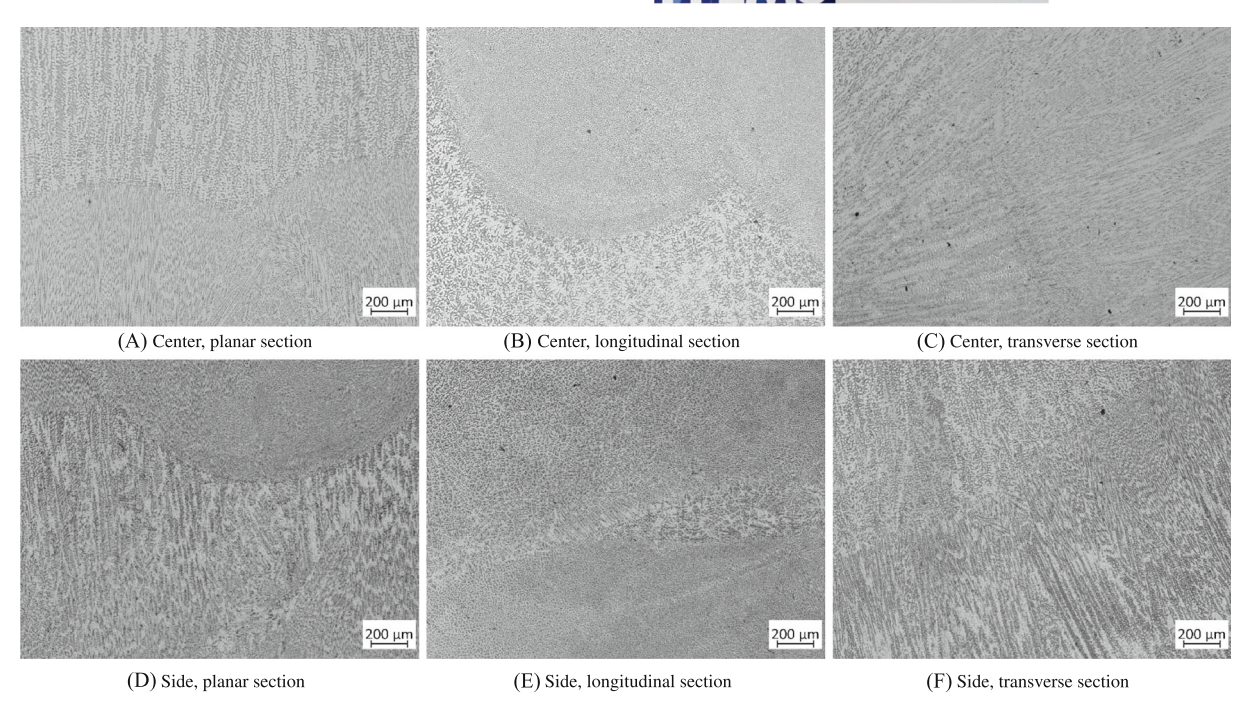
4 | RESULTS AND DISCUSSION

4.1 | Experimental results

This section reports and discusses the experimental data obtained from the tests performed.

Figure 6 depicts the results of the metallographic investigations made on the samples extracted at the location indicated in Figure 1. As presented in the previous section, the samples are ground and polished, and subsequently etched into an electrolytic compound for 30 s. The heterogeneity in the microstructure allows identifying the weld beads in every surface orientation analyzed, and it appears to be more pronounced in the planar section, that is, Figure 6A,D. The microstructure develops from coarse grains, with the presence of δ -ferrite both with lacy and vermicular morphology, to fine columnar

4602695, 2024, 11, Downloaded from https://onlinelibrary.wiley.com/doi/10.1111/fe.14430 by Tho Ris, Wiley Online Library on [06/12/2024]. See the Terms and Conditions (https://onlinelibrary.wiley.com/terms-ad-conditions) on Wiley Online Library for rules of use; OA articles are governed by the applicable Creative Commons Licenses



Optical micrographs for the specimens located at the center of the plate (A-C) and at the side of the plate (D-F).

grains oriented parallel to the building direction, confirming the results in Haden et al,³⁷ among others. The inhomogeneous and layered microstructure is the cause of the anisotropy of the material, which has been previously observed in the literature.³⁰ For uniaxial stress calculation conducted in the transverse direction, like in the present investigation, the material can be assumed as elastic and isotropic due to material symmetry. The printing strategy reported in Table 1 results in δ -ferrite having vermicular morphology in the longitudinal section, as shown in Figure 6B, where columnar grains are evident in the area with finer grains. The columnar grains are more evident in the transverse section, Figure 6C, where the separation of morphology due to the weld line becomes much sharper than in the longitudinal section, where a transition zone can be recognized. The samples extracted from the side of the plate show similar features as those observed from the samples extracted from the center of the plate. The material shows no significant defects, except for some porosity potentially caused by a lack of cleaning between layers, as delineated for AISI 316L in Queguineur et al. 38 Considering the findings in the literature, ^{37,39} this material could be categorized as a low-defect material due to the absence of pores having an area larger than 0.5 µm².

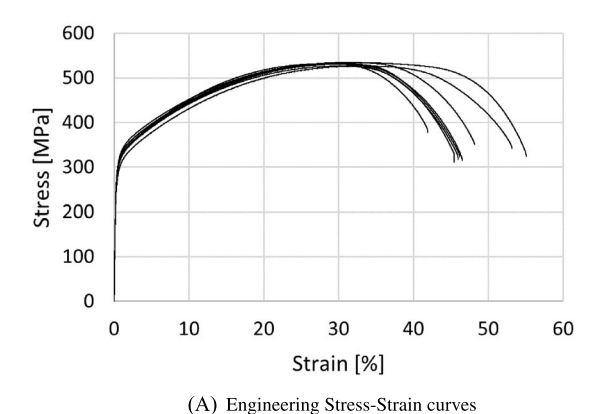
Table 2 reports the results of static tensile tests and Vickers Hardness. The average value of Vickers Hardness across nine measurements made in the section corresponding to the building plane (166 HV) is comparable with the value obtained in Singh et al⁴⁰ for

304L butt welds (170 HV). On the contrary, the average value of Vickers Hardness ranges between 202 to 211 for AISI 304 in Haden et al,³⁷ and it depends on the position, suggesting increasing strength with the building direction.

Figure 7A compares the resulting engineering stressstrain curves for the eight tensile tests conducted. The results agree with those reported in other studies. 20,30,41 The corresponding stress rate is calculated for the linear elastic regime considering the signal acquired by the force transducer, the measured cross-section area, and the time stamp resulting from the data acquisition. Table 2 reports the static tensile properties. The Young Modulus is measured according to the procedure and the indications in the ASTM E8M³¹ and ASTM E3076⁴² standards. The reason for which the value is significantly lower than typical ferritic steels has been associated with the fact that the FCC-cubic crystal structure of stainless steels is anisotropic and its elastic modulus varies in the range of 101-297 GPa, depending on the crystal direction.³⁰ The proportionality limit appears 27% smaller than the 0.2% proof stress, as shown in Figure 7B. This limits the applicability of the linear elastic material model for the examined material to a significantly smaller domain than that identified by the 0.2% proof stress. The proportionality limit has been identified as the lowest stress value for which the difference between the strain predicted by the Hooke law and the engineering stress-strain curve is, for larger values, always greater than three times the standard deviation obtained by

TABLE 2 Results of static tensile and hardness tests.

Specimen ID	Max. force P _{max} (kN)	Young modulus E (MPa)	UTS σ_u (MPa)	0.2% proof stress $\sigma_{p,0.2}$ (MPa)	Proportional limit $\sigma_{p,l}$ (MPa)	Strain at UTS ε_u (mm/mm)	Strain at fracture ε_f (mm/mm)	Vickers hardness HV1 (kgf/mm²)
T1	33.51	117419	527	272	185	0.33	0.53	
T2	34.02	122224	535	284	195	0.33	0.55	
T3	34.03	117402	535	285	198	0.31	0.48	
T4	33.88	139342	533	282	218	0.28	0.42	
T5	33.59	117696	528	294	221	0.30	0.46	
T6	33.90	120539	533	297	219	0.30	0.47	
T7	33.58	125113	528	284	201	0.30	0.45	
T8	33.87	130675	532	285	239	0.30	0.46	
	Mean	123801	531	285	210	0.31	0.48	166
	st err	2747	1.14	2.68	6.25	0.0058	0.015	0.51
	CoV	0.06	0.01	0.03	0.08	0.05	0.09	0.01



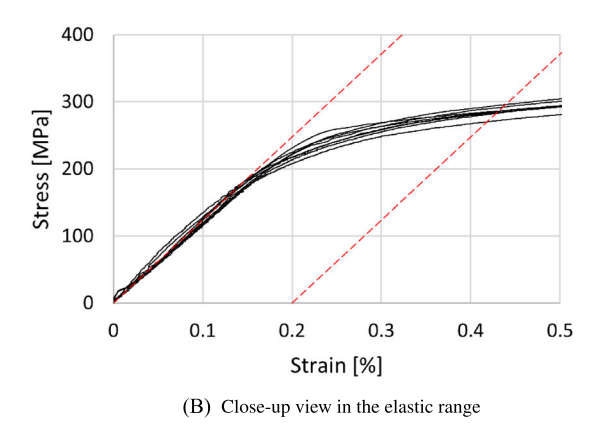


FIGURE 7 Engineering stress-strain curves for the examined material. [Colour figure can be viewed at wileyonlinelibrary.com]

considering the stress levels smaller than the considered value. A sensitivity study conducted on the choice of such a threshold value revealed that selecting either two or three times the standard deviation does not lead to an appreciable difference in the results, being smaller than 2%.

4.2 | Staircase test

The loading conditions for each test and the corresponding number of loading cycles are listed in Table 3. In particular, the applied bending moment, M, and the resulting stress amplitude, $\sigma_{a,f,R}$, are reported. The parameter δ indicates whether a test results in a failure, $\delta=1$, or nonfailure, $\delta=0$. At the end of the staircase test, nine specimens failed over thirteen tested

specimens. Therefore, following the procedure outlined in Section 2.2, the estimation of the endurance limit is performed by considering the specimens that did not fail, since these are the least. The mean of the stress amplitude corresponding to the endurance limit with a zero mean stress, that is, R=-1, is $\mathrm{E}[\sigma_{0,f,R}]=231$ MPa and the standard deviation is $\mathrm{SD}[\sigma_{0,f,R}]=10.8$ MPa. Assuming that the base-10 logarithm of the endurance limit is a random variable following a normal distribution with mean $\mu_X=\log_{10}(\mathrm{E}[\sigma_{0,f,R}])$ and scale parameter $s_X=\mathrm{SD}[\sigma_{0,f,R}]/\mathrm{E}[\sigma_{0,f,R}]$, the 95% confidence interval of the mean is estimated as⁴³

$$\left[\mu_X - t_{\alpha,n-1}\sqrt{\frac{s_X}{n}}; \mu_X + t_{\alpha,n-1}\sqrt{\frac{s_X}{n}}\right] \tag{10}$$

and is reported in Table 3

4602695, 2024, 11, Downloaded from https://online.library.wiley.com/doi/10.1111/fe.14430 by Tho Ris, Wiley Online Library on [06/12/2024]. See the Terms and Conditions, thtps://onlinelibrary.wiley.com/terms-and-conditions) on Wiley Online Library for rules of use; OA articles are governed by the applicable Creative Commons Licenses and Conditions (https://onlinelibrary.wiley.com/terms-and-conditions) on Wiley Online Library for rules of use; OA articles are governed by the applicable Creative Commons Licenses (https://onlinelibrary.wiley.com/terms-and-conditions) on Wiley Online Library for rules of use; OA articles are governed by the applicable Creative Commons Licenses (https://onlinelibrary.wiley.com/terms-and-conditions) on Wiley Online Library for rules of use; OA articles are governed by the applicable Creative Commons Licenses (https://onlinelibrary.wiley.com/terms-and-conditions) on Wiley Online Library for rules of use; OA articles are governed by the applicable Creative Commons Licenses (https://onlinelibrary.wiley.com/terms-and-conditions) on Wiley Online Library for rules of use; OA articles are governed by the applicable Creative Commons Licenses (https://onlinelibrary.wiley.com/terms-and-conditions) on Wiley Online Library for rules of use; OA articles are governed by the applicable Creative Commons Licenses (https://onlinelibrary.wiley.com/terms-and-conditions) on the applicable Creative Commons (https://onlinelibrary.wiley.com/terms-and-conditions) on the applicabl

Specimen number	<i>M</i> (N m)	$\sigma_{a,f,R}$ (MPa)	N (cycles)	δ ~
RB1	13.1	260	71,850	1
RB2	10.4	250	119,882	1
RB3	9.9	240	10,000,000	0
RB4	10.4	250	199,295	1
RB5	9.9	240	2,273,960	1
RB6	9.5	230	324,830	1
RB7	9.1	220	10,000,000	0
RB8	9.5	230	10,000,000	0
RB9	9.9	240	214,849	1
RB10	9.5	230	156,297	1
RB11	9.1	220	10,000,000	0
RB12	9.5	230	322,730	1
RB13	9.1	220	10,000,000	0
RB14	9.5	230	376,283	1
Endurance	Mean	95% CI of	mean	
limit	(MPa)	(MPa)		
$\sigma_{0,f,R}$	231	[202, 264]		
$(*)\delta = 1$ failure	e; δ =0 no fail	ure		

4.3 Analysis of the fracture surfaces

The fracture surfaces of the fatigue specimens n. 14 and n. 7 are analyzed, both having as-built surfaces but the former tested under a load ratio R = 0.1 and relatively low stress range, that is, 156MPa, and the latter tested under a load ratio R = 0.5 and higher stress range, that is, 300MPa. This examination aims to study the effect of the as-built surface and surface defects such as weld spatters on the failure mechanisms. Figure 8A,B shows two locations on the fracture surface of specimen n. 14, indicating multiple crack initiation sites at the surface, consistent with the expectation at low applied load. These initiation sites do not coincide with a weld spatter. Figure 8A shows a magnification of a weld spatter below which a beachmark is present at a depth of approximately equal to 1 mm from the surface. In addition, multiple ratchet marks are visible, indicating the coalescence of multiple cracks initiated along the notch root. Below the beachmark, some internal defects are visible as dark circular areas. This fractography suggests that these subsuperficial defects do not trigger crack initiation and that fatigue failure is induced by cracks initiating at the free surface of this specimen. Figure 8C shows another crack initiation location at the free surface appearing like a valley on the fracture surface.



The same can be observed for specimen n. 7 in Figure 8D, where a deep valley can be seen on the fracture surface of the upper section of the specimen. The fracture surface of the upper half of specimen n. 7, which has been tested at a higher load ratio and load level than specimen n.14, is then inspected. Since specimen n. 7 is loaded with a relatively high stress range, a leading crack is expected to lead to the final fracture of the specimen. However, as can be seen from Figure 8E, multiple initiation sites are found from the surface, similar to the previous specimen. Figure 8E shows the nucleation zone and the first phase of crack propagation. The morphology of the crack propagation zone is shown in Figure 8F, which is evident from the "orange peel" appearance. The appearance of the fracture surface in the region of the final fracture is shown in Figure 8G. These images confirm the ductile behavior of this material during the different fatigue stages, and also that the fatigue failure is induced by cracks nucleating at the free surface.

Results of fatigue tests

Table 4 reports the fatigue test results where, for each specimen, the nominal cross-section area A_{nom} , the nominal stress range $\Delta \sigma_{nom,R}$, the number of cycles to complete fracture N and the failure indicator δ are given. Figure 9A shows the experimental results obtained for a load ratio R = 0.1 for both as-built and smooth specimens. The Basquin equation is used to infer the failure data by using the least square method. Considering $x = \log_{10}(\Delta \sigma_{nom,R})$ as the independent variable and $y = \log_{10}(N)$ as the dependent one, the least square method can be applied to estimate the parameters a and m of the Basquin equation in a logarithmic format:

$$\log_{10}(N) = a + m \cdot \log_{10}(\Delta \sigma_{nom,R}) \tag{11}$$

The standard deviation of the base-10 logarithm fatigue life, s_Y , is estimated by evaluating the mean of the residuals squared, that is, $\epsilon^2 = (\hat{\mu}_{Y|x} - \log_{10}(N_i))^2$, thereby assuming the scatter being independent of the load level, that is, homoscedasticity. To estimate the residual, $\hat{\mu}_{Y|x}$ = $\log_{10}(\hat{N})$ is evaluated by using Equation (11) and considering the estimators of the model parameters, that is, \hat{m} and \hat{a} . Due to the limited number of fatigue test data, the uncertainty underlying the estimation of the model parameters is considered by estimating a $100(1-\alpha)\%$ confidence interval about the mean response $\hat{\mu}_{Y|x}$ at the stress level x_i^{43} :

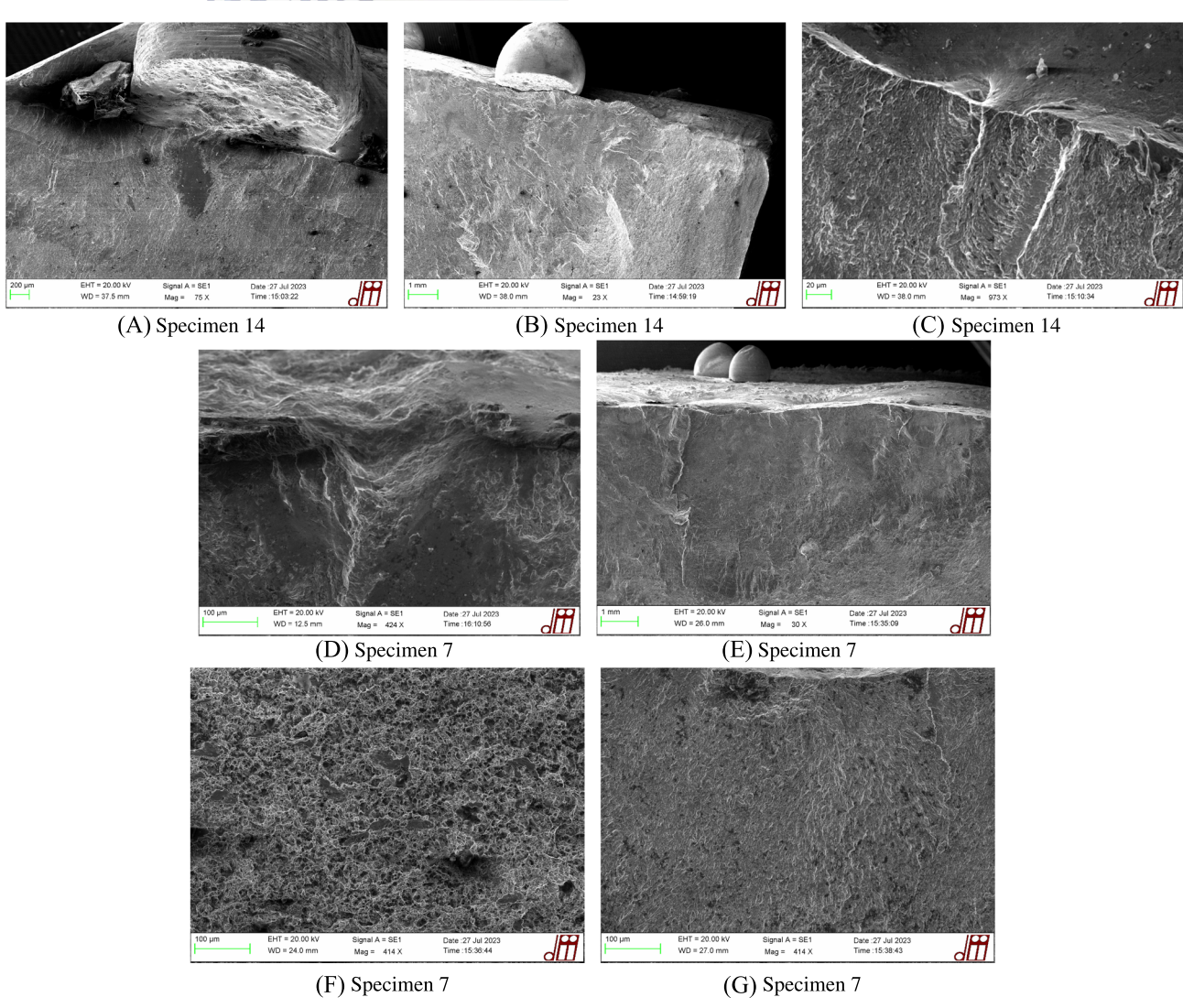


FIGURE 8 SEM pictures of the fracture surface of specimens 14 and 7. [Colour figure can be viewed at wileyonlinelibrary.com]

$$\left[\hat{\mu}_{Y|x} - t_{\alpha/2, n-2} \cdot \sqrt{s_Y^2 \left[\frac{1}{n} + \frac{(x_i - E[x])^2}{S_{xx}} \right]}; \\
\hat{\mu}_{Y|x} + t_{\alpha/2, n-2} \cdot \sqrt{s_Y^2 \left[\frac{1}{n} + \frac{(x_i - E[x])^2}{S_{xx}} \right]} \right]$$
(12)

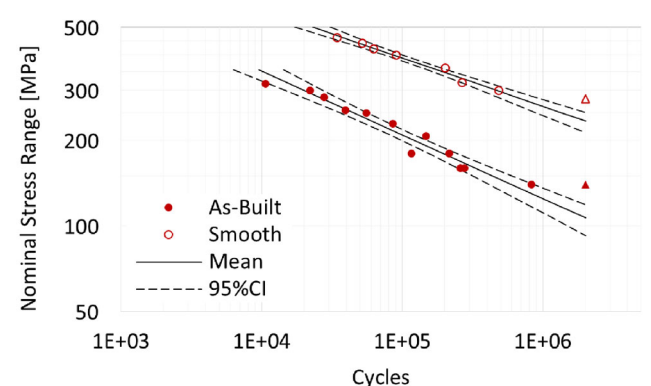
in which $t_{\alpha/2,n-2}$ is the value of the two-sided Student's t distribution evaluated at $\alpha/2$, and considering n-2 degrees of freedom, x_i is the base-10 logarithm of the stress range, E[x] is the base-10 logarithm of the nominal stress range corresponding to the centroid of the dataset, and $S_{xx} = \sum_n (x - E[x])^2$, where n is the number of data used to fit the Basquin equation. The mean regression curve and its 95% confidence interval are estimated and they are shown in Figure 9A. As shown in this figure, the 95% confidence interval of the mean S-N curve increases depending on the difference between the considered

logarithm of the stress level, x_i , and the average of logarithm of the stress level applied to each specimen E[x]. Table 5 summarizes the linear regression model results for all the datasets.

Figure 9B shows a comparison between the S-N curves obtained for the specimens containing the as-built surface tested at two load ratios, that is R=0.1 and R=0.5. The failure data are inferred by using the Basquin equation, where the estimators and main results are reported in Table 5. The comparison suggests that the dependency of the mean stress effect depends on the applied stress range for the selected geometry. The S-N curves seem to overlap toward low cycle fatigue, that is, N approaching 10^3 cycles, whereas a larger difference is present at lower stress ranges. This agrees with what others have observed for metals in general, and it also agrees with Morrow's mean stress correction rule applied to the Coffin–Manson–Basquin equation.⁷

ABLE 4	Fatigue test	resurts.		
#	A_{nom} (mm ²)	$\Delta \sigma_{nom,R}$ (MPa)	N (cycles)	$\delta^{(*)}$
Smooth sp	pecimens - R =	0.1		
1	167.5	300	483,948	1
2	168.9	400	90,580	1
3	166.7	320	265,773	1
4	168.0	420	62,798	1
5	168.0	440	51,996	1
6	170.1	460	34,279	1
7	168.4	280	2,000,000	0
8	168.6	360	201,031	1
As-built s	pecimens - R =	0.1		
1	172.7	316	10,641	1
2	167.7	285	27,860	1
3	169.7	256	39,328	1
4	166.8	230	85,926	1
5	163.8	207	146,849	1
9	243.2	180	116,195	1
10	239.1	180	215,441	1
11	232.9	160	259,619	1
12	235.5	160	275,082	1
13	232.5	140	2,000,000	0
14	237.8	140	826,037	1
21	236.1	300	21,947	1
22	229.7	250	55,699	1
As-built s	pecimens - R =	0.5		
7	177.6	300	7265	1
6	169.3	200	104,486	1
8	166.4	250	50,716	1
15	231.2	250	56,896	1
16	235.9	200	79,993	1
17	235.3	180	172,195	1
18	241.9	180	151,300	1
19	229.1	160	155,774	1
20	31.8	160	102,189	1
23	233.8	120	199,256	1
24	233.8	80	1,485,874	1
25	233.8	120	213,607	1
26	233.8	80	2,000,000	0
$(*)\delta - 1$ fa	ilure; $\delta = 0$ no	failure		

By assuming the presence of residual stresses, the effective stress ratio for linear elastic material $R_{eff,el}$ is calculated as



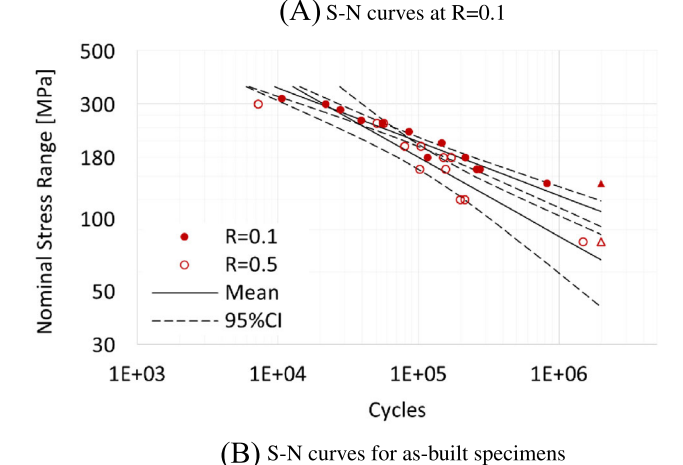


FIGURE 9 S-N curves obtained for smooth and as-built specimens. Right censored data (runouts) are indicated with a triangle. [Colour figure can be viewed at wileyonlinelibrary.com]

$$R_{eff,el} = \frac{\sigma_{minf,R} + \sigma_{res}}{\sigma_{max,f,R} + \sigma_{res}}$$
 (13)

where $\sigma_{min,f,R}$ and $\sigma_{max,f,R}$ are the local fatigue notch stresses at the notch root at minimum and maximum applied load, respectively, and σ_{res} is the residual stress. The fatigue notch stress is $\sigma_{a,f,R} = K_f \cdot \sigma_{nom}$. In the presence of elastic shakedown, and by assuming an elastic perfectly plastic material, that is, when $\sigma_{max,f,R}$ + $\sigma_{res} > \sigma_{p,0.2}$ and $\sigma_{a,f,R} < \sigma_{p,0.2}$, the effective mean stress can be determined by assuming that the maximum stress does not exceed the yield stress, see Equation (8). Therefore, depending on the relative magnitude of residual stresses and their potential relaxation, elastic shakedown takes place at relatively high load levels, determining the fact that the effective load ratio is independent of the load ratio of the applied load. By decreasing the stress ranges, the effective load ratio increases approaching to R, and tends to unity for the applied stress ranges reaching zero. However, these cases are not relevant. The 95% confidence intervals of the mean S-N curves obtained for R = 0.1 and R = 0.5 do not overlap at the endurance

limit, that is, at 2 million cycles. This suggests that the endurance limits obtained for R=0.1 and R=0.5 are not statistically comparable.

As presented in Section 3.2, the fatigue notch factor, K_f , is defined as the ratio between the nominal stress ranges for smooth and as-built specimens corresponding to the endurance limit. By considering the endurance limit as the stress range corresponding to a fatigue life of 2 million loading cycles, the endurance limit is determined by using the S-N curves shown in Figure 9A. Therefore, the endurance limit, $\Delta \sigma_{0.nom}$, is also reported in Table 5. By considering the mean estimators, the fatigue notch factor K_f resulting from the experiments is equal to 2.2. Due to the uncertainty underlying the estimation of the mean regression curve, the estimation of the mean endurance limit, and hence the fatigue notch factor, are also subject to uncertainty. The Monte Carlo method is used to estimate the 95% confidence interval of the mean estimator of the fatigue notch factor. This procedure aims to find the value $x_0 = \log_{10} \Delta \sigma_{0,nom}$ that makes true the following equality:

$$log(2 \cdot 10^{6}) = \hat{a} + \hat{m} \cdot x + t_{n-2} \cdot \sqrt{\hat{s}_{Y}^{2} \left[\frac{1}{n} + \frac{(x_{0} - E[x])^{2}}{S_{xx}} \right]}$$
(14)

in which t_{n-2} is a randomly sampled value of the Student's t distribution, with n-2 degrees of freedom. Each determination is repeated a large number of times (10^6) with different values of t_{n-2} and by considering the S-N curve parameters resulting from the inference of the test data produced for as-built and smooth specimens at R=0.1. The resulting 95% confidence intervals for the mean of the endurance limit of as-built and smooth specimens are reported in Table 6. Note that this numerical

approach is needed because the confidence interval estimator of the fatigue resistance for a certain fatigue life does not have a closed-form solution. The ratio of each randomly sampled value of the endurance limit for smooth and as-built specimens is a random determination of the fatigue notch factor, considering the uncertainty resulting from the test data. As a result of this procedure, the 95% confidence interval of the mean value of the fatigue notch factor is reported in Table 6.

4.5 | Numerical prediction of fatigue notch factor for as-build components

This section presents the fatigue notch factor estimated by using the FE model and the procedure described in Sections 3.1 and 3.2. The fatigue notch factor is determined in 19 locations, each of them corresponding to the most stressed location in the submodel. The submodels are extracted as portions of the plate modeled in the global model, see Figure 4. In particular, the submodel is extracted along the center of the plane identified along the building direction. Moreover, since its size might affect the fatigue notch factor, due to statistical weakest link effects, the width of the submodel is that of the specimens used for the fatigue tests. Table 6 summarizes the results of the finite element model. The fatigue notch factor estimated numerically is on average 0.9 times the one estimated expectation through the experiments. Hence, this is within the 95% confidence interval of the mean fatigue notch factor determined by the experiments.

The fatigue notch factor obtained through the FE model, together with the S-N curve on smooth specimens, is used to predict the fatigue lives of the as-built condition. The confrontation of this prediction with the experimentally obtained data in as-build condition allows to further evaluate the goodness of the fatigue notch

Dataset	R (-)	n (-)	$\hat{m{a}}$ $(-)$	m (-)	\hat{s}_Y (MPa)	R ² (-)	$\Delta \sigma_{0,nom}$ (MPa)
As-built	0.1	12	15.36	-4.463	0.129	0.95	107
Smooth	0.1	7	20.24	-5.880	0.062	0.98	235
As-built	0.5	12	11.85	-3.036	0.227	0.83	67

TABLE 5 Parameters of the S-N curves for the three considered datasets.

As-built	Smooth	Experiment	FE model		
$\mathbf{E}[\Delta\sigma_{0,nom}]$ (MPa)	$\mathbf{E}\left[\Delta\sigma_{0,nom} ight]$ (MPa)	K_f $(-)$	K_t $(-)$	K_f $(-)$	n_{σ} $(-)$
235	107	2.2	2.5	2.0	0.8
(218; 248)	(95.7; 117)	(1.95; 2.49)	(2.2; 2.9)	(1.8; 2.2)	

TABLE 6 Notch effect of surface waviness.

4602695, 2024, 11, Downloaded from https://onlinelibrary.wiley.com/doi/10.1111/ffe.14430 by Tho Ris, Wiley Online Library on [06/12/2024]. See the Terms and Conditions (https://onlinelibrary.wiley.com/remv

and-conditions) on Wiley Online Library for rules of use; OA articles

are governed by the applicable Creative Commons License

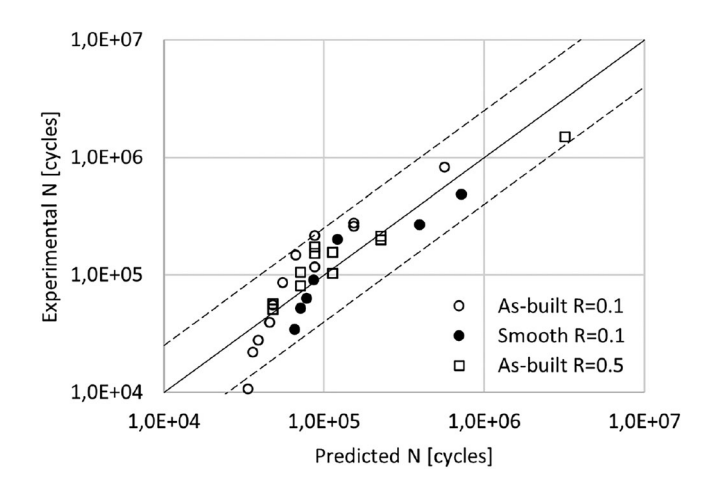


FIGURE 10 Correlation between experimental and predicted fatigue life.

factor. The aim is to further evaluate the goodness of the fatigue notch factor. Hence, by considering both the average value of K_f and a mean stress correction rule, the local fatigue stress can be calculated for all the test specimens for a unique stress ratio that, for simplicity, is set to R = -1. The correction for K_f is applied to all the data points in virtue of the fact that the S-N curves for as-built and smooth specimens are parallel to each other, see Figure 9A.

By calculating $\sigma_{a,f,R}$ at R=-1 for all the experimental data points, the agreement with the experimental data is evaluated in terms of linear regression. The Basquin equation is fitted to the transformed dataset, that is, considering $x = \log_{10}(\sigma_{a,f,R=-1})$, and $y = \log_{10}(N)$, obtained from the pooling of the three datasets presented in Section 4.4. The obtained mean regression line is characterized by a coefficient of determination $R^2 = 0.76$ which is comparable to the lowest one obtained by inferring the test data presented in Table 5. Figure 10 shows a comparison between the experimental fatigue life and the fatigue life predicted by the obtained Basquin equation for the transformed dataset. The dashed lines correspond to a $(\pm 2\sigma)$ interval considering $\sigma = 0.2$, which is a typical value for the scatter of fatigue test on welded joints and similar to that one estimated for the tests conducted at R = 0.5. All experimental data except one are within the constructed scatter band, thus validating the numerical fatigue notch factor and the Goodman mean stress correction rule in combination with elastic shakedown correction.

CONCLUSIONS

This study focuses on the determination of the fatigue notch factor due to the surface waviness in WAAMed

AISI 308 LSi stainless steel specimens. Hence, three series of fatigue tests are carried out on specimens opportunely designed to induce fatigue failure within the as-built surface. As compared to other studies, the specimens are characterized by larger thickness, hence produced by a zig-zag pattern, and not a single layer. For the fatigue tests, two stress ratios have been considered, namely, R = 0.1, 0.5. A statistical description of the fatigue notch factor is inferred by comparing the endurance limit estimated from S-N curves obtained for machined and asbuilt specimens. The comparison shows that the fatigue notch factor, K_f is equal to 2.2. The same plates used for testing have been scanned by using a high-resolution laser scanner in order to develop a finite element model allowing the prediction of the stress concentration resulting from the as-built surface. The results of the finite element model allow to estimate a stress concentration factor that on average is equal to $K_t = 2.5$. By making use of the results of the finite element model, the fatigue notch factor is estimated by using the gradient correction provided in the FKM guideline,²⁷ leading to an average numerical estimation of the fatigue notch factor $K_f = 2.0$. As a result of the study, the predicted value of the fatigue notch factor is statistically comparable with that experimentally found. Moreover, it has been shown that by using a local stress approach, it is possible to correlate fatigue test results carried out under different stress ratios and surface conditions.

 a_G, b_G

LATURE					
fatigue notch factor					
theoretical stress concentration factor					
stress amplitude at endurance limit, given R					
maximum stress for fatigue calculation,					
given R					
minimum stress for fatigue calculation,					
given R					
mean stress for fatigue calculation, given R					
nominal stress amplitude at endurance limit,					
given R					
stress amplitude for fatigue, given R					
stress amplitude considering theoretical					
stress, given R					
distance between node p and point k					
stress gradient according to FKM					
K_f/K_t ratio according to FKM					
maximum principal stress at node p					
maximum principal stress at point k					
plane director cosines					
coordinates of node p					
coordinates of point k					

material parameters according to FKM

confidence level



 σ_u ultimate tensile stress $\sigma_{p,0,2}$ 0.2% proof stress

 σ_{nom} nominal stress in the cross section $\Delta \sigma_{nom,R}$ nominal stress range, given R

R stress ratio

 R_{eff} effective stress ratio E[-] expectation operator SD[-] standard deviation operator

 μ_X mean of logarithm of stress amplitude

(range)

x standard deviation of logarithm of stress

amplitude (range)

 $t_{\alpha,dof}$ value of Student's t distribution

nNumber of test dataMBending moment δ Failure indicator

 $\sigma_{p,l}$ Limit of proportionality

E Young's modulus P_{max} maximum applied force

 ε_u strain at ultimate tensile stress

 ε_f strain at fracture

HV1 Vickers hardness for 1 kgf

 A_{nom} nominal (minimum) area in test specimens

N number of cycles to failure a, m parameters of Basquin equation R^2 coefficient of determination

 ϵ residual in linear regression model $\mu_{Y|x}$ mean of logarithm of fatigue life given x standard deviation of logarithm of fatigue

life

x Base 10 logarithm of the stress range

(amplitude)

 S_{xx} sum of the squares of the difference between

x and E[x]

 σ_{res} residual stress

 $\Delta\sigma_{0.nom.R}$ nominal stress range at the endurance limit,

given R

AUTHOR CONTRIBUTIONS

Davide Leonetti: Conceptualization; formal analysis; funding acquisition; methodology; supervision; writing—original draft preparation. **Elena Zancato**: Formal analysis; investigation; methodology; visualization; writing—review & editing. **Giovanni Meneghetti**: Conceptualization; supervision; writing—review & editing. **Johan Maljaars**: Conceptualization; supervision; writing—review & editing.

ACKNOWLEDGEMENTS

The authors would like to thank the company MX3D for providing the material used in this study. In addition, we would also like to thank Mark Luijbregts from Lec3D for granting access to their metrology laboratory.

CONFLICT OF INTEREST STATEMENT

The authors declare no potential conflict of interest.

SUPPORTING INFORMATION

Additional supporting information may be found in the online version of the article at the publisher's website.

DATA AVAILABILITY STATEMENT

The data that support the findings of this study are available from the corresponding author upon reasonable request.

ORCID

Davide Leonetti https://orcid.org/0000-0002-7436-3977

Elena Zancato https://orcid.org/0009-0004-3656-5158

Giovanni Meneghetti https://orcid.org/0000-0002-4212-2618

Johan Maljaars https://orcid.org/0000-0001-5831-2478

REFERENCES

- Busachi A, Erkoyuncu J, Colegrove P, Martina F, Ding J. Designing a WAAM based manufacturing system for defence applications. *Procedia Cirp*. 2015;37:48-53.
- 2. Müller J, Grabowski M, Müller C, et al. Design and parameter identification of wire and arc additively manufactured (WAAM) steel bars for use in construction. *Metals*. 2019; 9(7):725.
- 3. Omiyale BO, Olugbade TO, Abioye TE, Farayibi PK. Wire arc additive manufacturing of aluminium alloys for aerospace and automotive applications: a review. *Mater Sci Technol.* 2022; 38(7):391-408.
- Pant H, Arora A, Gopakumar GS, Chadha U, Saeidi A, Patterson AE. Applications of wire arc additive manufacturing (WAAM) for aerospace component manufacturing. *Int J Adv Manuf Techny*. 2023;127(11-12):4995-5011.
- Taşdemir A, Nohut S. An overview of wire arc additive manufacturing (WAAM) in shipbuilding industry. Ships and Offshore Struct. 2021;16(7):797-814.
- Martina F, Mehnen J, Williams SW, Colegrove P, Wang F. Investigation of the benefits of plasma deposition for the additive layer manufacture of Ti-6Al-4V. J Mat Process Technol. 2012;212(6):1377-1386.
- Suresh S. Fatigue of Materials: Cambridge university press; 1998.
- 8. Geng H, Li J, Xiong J, Lin X, Huang D, Zhang F. Formation and improvement of surface waviness for additive manufacturing 5a06 aluminium alloy component with GTAW system. *Rapid Prototyp J.* 2018;24(2):342-350.
- Chernovol N, Sharma A, Tjahjowidodo T, Lauwers B, Van Rymenant P. Machinability of wire and arc additive manufactured components. CIRP J Manuf Sci Technol. 2021;35:379-389.
- 10. Dirisu P, Supriyo G, Martina F, Xu X, Williams S. Wire plus arc additive manufactured functional steel surfaces enhanced by rolling. *Int J Fatigue*. 2020;130:105237.
- 11. Biswal R, Zhang X, Syed AK, et al. Criticality of porosity defects on the fatigue performance of wire+ arc additive manufactured titanium alloy. *Int J Fatigue*. 2019;122:208-217.

- Beretta S, Gargourimotlagh M, Foletti S, Du Plessis A, Riccio M. Fatigue strength assessment of "as built" AlSi10Mg manufactured by SLM with different build orientations. *Int J Fatigue*. 2020;139:105737.
- 14. Maddox SJ. Fatigue Strength of Welded Structures: Woodhead Publishing; 2014.
- 15. Akgun E, Zhang X, Biswal R, Zhang Y, Doré M. Fatigue of wire+arc additive manufactured Ti-6Al-4V in presence of process-induced porosity defects. *Int J Fatigue*. 2021;150: 106315.
- Bercelli L, Moyne S, Dhondt M, Doudard C, Calloch S, Beaudet J. A probabilistic approach for high cycle fatigue of wire and arc additive manufactured parts taking into account process-induced pores, 42; 2021.
- 17. Ermakova A, Razavi N, Berto F, Mehmanparast A. Uniaxial and multiaxial fatigue behaviour of wire arc additively manufactured ER70S-6 low carbon steel components. *Int J Fatigue*. 2023;166:107283.
- Hensel J, Müller J, Scharf-Wildenhain R, Uhlenberg L, Hälsig A. The effects of building position on surface and fatigue of DED-arc steel components. Weld World. 2023;67(4):859-872.
- Huang C, Li L, Pichler N, Ghafoori E, Susmel L, Gardner L. Fatigue testing and analysis of steel plates manufactured by wire-arc directed energy deposition. *Addit Manuf.* 2023;73: 103696.
- Leonetti D, de Munnik M, Kassing L, Khan D, Moulin J-F, Snijder B. Rotating bending fatigue behaviour and quasi-static tensile properties of wire arc additively manufactured 308l stainless steel. ce/papers. 2023;6(3-4):732-738.
- Zancato E, Leonetti D, Meneghetti G, Maljaars J. Experimental evaluation of the fatigue notch factor in as-built specimens produced by wire and arc additive manufacturing. *Procedia Struct Integr.* 2024;53:315-326.
- 22. Bartsch H, Kuehne R, Citarelli S, Schaffrath S, Feldmann M. Fatigue analysis of wire arc additive manufactured (3D printed) components with unmilled surface. *Structures*: Elsevier; 2021:576-589.
- 23. Fricke W. IIW recommendations for the fatigue assessment of welded structures by notch stress analysis: IIW-2006-09. In: Fricke W, ed. IIW Recommendations for the Fatigue Assessment of Welded Structures by Notch Stress Analysis: Woodhead Publishing Series in Welding and Other Joining Technologies. Woodhead Publishing; 2012.
- 24. Kranz B, Sonsino CM. Verification of FAT values for the application of the notch stress concept with the reference radii $R_{\rm ref}=1.00$ and 0.05 mm. Welding World. 2010;54:R218-R224.
- Shamir M, Zhang X, Syed AK, Sadler W. Predicting the effect of surface waviness on fatigue life of a wire+ arc additive manufactured Ti-6Al-4V alloy. *Materials*. 2023;16(15):5355.
- 26. Radaj D, Sonsino CM, Fricke W. Fatigue Assessment of Welded Joints by Local Approaches: Woodhead Publishing; 2006.
- 27. Herausgeber FKM. Analytical Strength Assessment 7th Ed. 2020: VDMA Verlag; 2020.
- MX3D company description. https://mx3d.com/company/ about/ Accessed: 31/07/2024.

- 29. Belotti LP, van Dommelen J, Geers MG, Ya W, Hoefnagels JM. Influence of the printing strategy on the microstructure and mechanical properties of thick-walled wire arc additive manufactured stainless steels. *J Mat Process Technol.* 2024;324: 118275.
- Laghi V, Tonelli L, Palermo M, et al. Experimentally-validated orthotropic elastic model for wire-and-arc additively manufactured stainless steel. *Addit Manuf*. 2021;42:101999.
- 31. ASM International. ASTM E8/E8M Standard Test Methods for Tension Testing of Metallic Materials. ASTM International, West Conshohocken, PA; 2021.
- ASM International. ASTM E3-11 Standard Guide for Preparation of Metallographic Specimens. ASTM International, West Conshohocken, PA; 2011.
- Castagnetti D, Dragoni E. Stress concentrations in periodic notches: a critical investigation of Neuber's method. *Material-wiss Werkst.* 2013;44(5):364-371.
- ASM International. ASTM E466-21 Standard Practice for Conducting Force Controlled Constant Amplitude Axial Fatigue
 Tests of Metallic Materials. ASTM International, West Conshohocken, PA; 2021.
- ANSYS Inc. ANSYS Mechanical User's Guide. Release 2023R2;
 2023.
- PolyWorks. Polyworks Inspector Measurement and Verification Software. Release 2017; 2017.
- 37. Haden CV, Zeng G, Carter III FM, Ruhl C, Krick B, Harlow D. Wire and arc additive manufactured steel: tensile and wear properties. *Addit Manuf.* 2017;16:115-123.
- 38. Queguineur A, Rückert G, Cortial F, Hascoët JY. Evaluation of wire arc additive manufacturing for large-sized components in naval applications. *Welding World*. 2018;62(2):259-266.
- 39. Ge J, Lin J, Chen Y, Lei Y, Fu H. Characterization of wire arc additive manufacturing 2cr13 part: process stability, microstructural evolution, and tensile properties. *J Alloy Compd.* 2018;748:911-921.
- 40. Singh PJ, Guha B, Achar DRG. Fatigue life prediction for aisi 304l butt welded joints having different bead geometry using local stress approach. *Sci Technol Weld Join*. 2003;8(4):303-308.
- 41. Kyvelou P, Slack H, Mountanou DD, et al. Mechanical and microstructural testing of wire and arc additively manufactured sheet material. *Mater Des.* 2020;192:108675.
- ASM International. ASTM E3076-10 Standard Practice for Determination of the Slope in the Linear Region of a Test Record. ASTM International, West Conshohocken, PA; 2010.
- 43. Montgomery DC, Peck EA, Vining GG. *Introduction to Linear Regression Analysis*: John Wiley & Sons; 2021.

How to cite this article: Leonetti D, Zancato E, Meneghetti G, Maljaars J. Experimental and numerical determination of the fatigue notch factor in as-built wire arc additive manufacturing steel components. *Fatigue Fract Eng Mater Struct*. 2024;47(11):4372-4389. doi:10.1111/ffe.14430